Efficient Minority Carrier Detrapping mediating the Radiation Hardness of Triple-Cation Perovskite Solar Cells under Proton Irradiation

Felix Lang[1], Marko Jošt[2], Jürgen Bundesmann[3], Andrea Denker[3,4], Steve Albrecht[2,5], Giovanni Landi[6,7], Heinz-Christoph Neitzert[6], Jörg Rappich[1], Norbert H. Nickel[1]*

[1]Helmholtz-Zentrum Berlin für Materialien und Energie GmbH, Institut für Silizium Photovoltaik, Kekuléstr. 5, 12489 Berlin, Germany.
[2]Helmholtz-Zentrum Berlin für Materialien und Energie GmbH, Young Investigator Group Perovskite Tandem Solar Cells, Kekuléstr. 5, 12489 Berlin, Germany
[3]Helmholtz-Zentrum Berlin für Materialien und Energie GmbH, Protonen für die Therapie, Hahn-Meitner Platz 1, 14109 Berlin, Germany
[4] Beuth Hochschule für Technik Berlin, Fachbereich II - Mathematik - Physik - Chemie, D-13353 Berlin, Germany
[5]Technical University Berlin, Faculty IV – Electrical Engineering and Computer Science, 10587 Berlin, Germany
[6]Dept. of Industrial Engineering (DIIn), Salerno University, Via Giovanni Paolo II 132, 84084 Fisciano (SA), Italy
[7]Institute for Polymers, Composites and Biomaterials, National Research Council of Italy, P. Enrico Fermi 1, 80055 Portici, Italy

* Dr. Felix Lang, fl396@cam.ac.uk

Keywords: perovskite solar cells, radiation hardness, proton irradiation, degradation, defects

Abstract: Highly efficient perovskite based solar cells have the potential to be a game-changing solar array technology for space applications that can be flexible, truly roll-able, ultra-lightweight and highly stowable. Outside earth's magnetic field, however, ionizing radiation causes localized defect states that accumulate and ultimately cause the failure of electronic devices. This study, assesses the radiation hardness of the widely used triple cation based perovskite absorber material, namely $Cs_{0.05}MA_{0.17}FA_{0.83}Pb(I_{0.83}Br_{0.17})_3$ employing 10, 20 and 68 MeV proton irradiation. Therefore, *in-situ* measurements of the degradation of the proton induced current as well as the photovoltaic performance during proton irradiation are used as two independent metrics. Both measurements suggest that triple cation perovskites even exceed the radiation hardness of SiC, which is a material often proposed to possess an excellent radiation hardness. Our optimized $Cs_{0.05}MA_{0.17}FA_{0.83}Pb(I_{0.83}Br_{0.17})_3$ based space solar cells reach efficiencies of 18.8 % under AM0 illumination and maintain 95 % of their initial efficiency even after irradiation with protons at an energy 68 MeV and a total dose of 10^{12} p/cm^2. Degradation under 10 and 20 MeV proton irradiation is even lower. Despite the negligible impact on solar cell device performance, this study identifies that proton irradiation is changing the recombination kinetics under low excitation densities profoundly. Dark capacitance-voltage and current-voltage characteristics, photoluminescence spectra as well as photoluminescence and V_{OC} decays are analyzed in depth. Surprisingly, two fold prolonged PL and V_{OC} decay times are observed after proton irradiation. Often, such prolongations are attributed to a reduced charge recombination. Our kinetic model, precisely describing the observed time evolution after photoexcitation, however, establishes the prolonged release of trapped minority charge carriers from proton-radiation induced trap states.

TOC figure

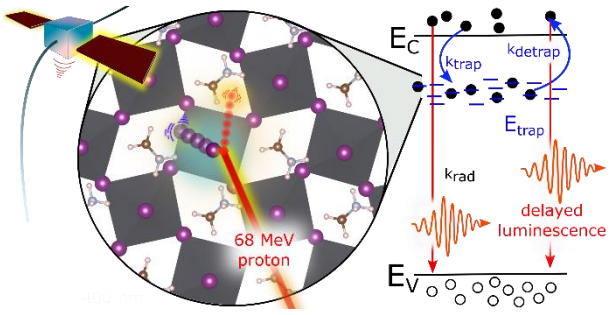

1. Introduction

Organic-inorganic perovskites are direct semiconductors that have recently proven to be ideal for numerous optoelectronic applications. Latest breakthroughs have been achieved by compositional engineering of the underlying AMX_3 structure.[1–3] While M and X are typically confined to divalent lead (Pb^{2+}) and a monovalent halide anion such as iodine (I^-) or (Br^-), the A cations are vastly mixed. Employed cations are rubidium (Rb^+), cesium (Cs^+), methylammonium ($CH_3NH_3^+$, MA) and formamidinium ($HC(NH_2)_2^+$, FA).[1–4] While this increases complexity immensely, the approach allows to compensate for thermal- and photo-instabilities.[5] Mixed double-, triple- or quadruple cation perovskites exhibit extraordinary low non-radiative recombination losses of $\Delta V_{oc} = E_g/e\text{-}V_{oc} \approx 0.39$ V[3] and charge carrier diffusion lengths of several μm[6]. Best performing perovskite solar cells reach power conversion efficiencies of $\eta \sim 23.7$ %.[7] This value is above other thin film technologies such as $Cu(In,Ga)Se_2$ at 22.9 % and approaches the world record of other single junction technologies, such as GaAs or Si with 29.1 % and 26.6 %, respectively.[8] Additionally, compositional engineering can be employed to tune the optical band gap of hybrid perovskites between 1.5 eV and 1.9 eV.[9] Consequently, perovskites are a good choice for multijunction solar-cells with ultrahigh efficiency. Perovskite/perovskite, Perovskite/silicon and perovskite/$Cu(In,Ga)Se_2$ tandem solar cells with efficiencies of 19.1 %[10], 25.5 %[11] and 22.4 %[12] have been demonstrated recently in monolithic design.

Modern satellites and spacecraft require several kW of electric power.[13] Typically this power is provided by solar arrays. In contrast to applications on earth, a high mass-specific power (W/kg) and a low stowed volume during launch are crucial parameters. For this reason, roll-out solar arrays (ROSA) have been developed, tested and used.[13–16] A prominent example is the international space station with one of the first ROSA arrays. However, in most cases, rigid solar cells based on crystalline silicon (single junction) or Ge/GaAs/GaInP (triple junction) are used. Consequently, current ROSA solar arrays are not as flexible and lightweight as they could be. Perovskite single junction as well as perovskite/perovskite and perovskite/$Cu(In,Ga)Se_2$ tandem solar cells can be fabricated and interconnected directly on large-area, ultra-thin polyimide foils.[17,18] This would enable a solar array technology that is highly efficient, truly roll-able, ultra-lightweight and highly stowable during launch. Moreover, studies by Brown et al. [19]

recently indicated that solar cells based on hybrid perovskites can work reliably in low-intensity-low-temperature (LILT) environments found Mars, Jupiter, or Saturn

Once launched into space, humans, spacecraft and satellites are bombarded by radiation comprising mainly protons (p) and electrons (e).[20] Electronic and nuclear interactions with the incident particles cause a variety of ionization and displacement effects in the absorber lattice. In earth's magnetosphere, the particle flux can vary between 10^3 and 10^8 particles $cm^{-2}\,s^{-1}$.[21] The highest flux, here, originate from particles that are trapped by earth's magnetic field in specific zones, the Van-Allen Belts. However, even outside the Van-Allen Belts it takes only 3 years to accumulate a substantial dose of 10^{12} particles cm^{-2}. At that dose, silicon, InGaP/GaAs as well as Ge/GaAs/GaInP solar cells that are typically used in space, degrade by around $25\%_{rel.}$ of the initial performance.[22–25] While $Cu(In,Ga)Se_2$ is one of the most radiation-resistant solar-cell absorber material[22], little is known on the radiation hardness of hybrid perovskites[5].

Recent investigations have tried to assess the radiation hardness of methylammonium lead iodide ($CH_3NH_3PbI_3$), the prototypical absorber composition in perovskite based solar cells.[26–29] However, power conversion efficiencies of the investigated $CH_3NH_3PbI_3$ based solar cells were low, ranging between 3 %[28,29] and 12 %[26,27]. Such un-optimized devices employ defect-rich absorber layers as well as non-ideal contact layers, both limiting the quasi-Fermi level splitting and consequently the open-circuit voltage (Voc). With such tremendous limitations, additional radiation-induced defects have no or only limited impact on device performance. With this in mind, it seems questionable if optimized perovskite single junction or top-cells in perovskite/$Cu(In,Ga)Se_2$ tandem solar cells would survive the extreme radiation environment in space. Some of the required double-, triple- or quadruple cation perovskites even tend to phase-separate into iodine and bromine-rich nanodomains under illumination.[9,30] Grounds for hope, are measurements by Yang et al.[31] who tested a triple cation perovskite under prolonged γ-Ray radiation. Radiation hard triple-cation perovskites would also enable X-Ray detectors for advanced real-time medical diagnostics[32,33] as well as sensors and transistors that work reliably in extremely radiation exposed environments such as operating or non-operating nuclear reactors

In this work, we, therefore, assess the radiation hardness of a triple cation based perovskite absorber material, namely $Cs_{0.05}MA_{0.17}FA_{0.83}Pb(I_{0.83}Br_{0.17})_3$ employing 10, 20 and

68 MeV proton irradiation. Investigated solar cells possess a high V_{OC} of ~ 1.13 V and low non-radiative recombination losses of $\Delta V_{oc} = E_g/e\text{-}V_{oc} \sim 0.49$ V. Efficiencies reach $\eta \sim 19$ % under both AM1.5 and AM0 conditions. *In-situ* measurements during proton irradiation as well as *ex-situ* measurements after proton irradiation suggest negligible degradation of solar cell device performance. Irradiated devices retain 95 % of their initial efficiency even at doses up to 10^{12} p/cm^2. Interestingly, our analyses suggest the formation of some radiation induced defect states causing an efficient trapping and detrapping of minority charge carriers without additional non-radiative recombination. This remarkable radiation resistance of a high efficiency perovskite solar cell is a quantum leap towards ultralight, flexible and highly stowable solar arrays that are predestinated for space. The derived understandings on the minority carrier trapping and detrapping in and from radiation induced defects states, further, may stimulate a different perspective on light-induced phenomena.

2. Radiation Hardness

To test for the radiation hardness of $Cs_{0.05}MA_{0.17}FA_{0.83}Pb(I_{0.83}Br_{0.17})_3$ we mimicked the harsh radiation environment in space by employing high energetic proton irradiation. This is more than adequate as electron irradiation induces about two orders of magnitude less damage.[28] The stopping range of high energetic protons is a function of their energy and therefore tests employing only one proton energy are insufficient. Consequently, we have chosen proton energies of 10 ± 3, 20 ± 3 and 68 ± 1 MeV. Those energies reflect the energy distribution of protons in space relatively well.[21] Protons with higher energies were not accessible experimentally but they are also less common in space.[21] Only on rare occasions, massive solar flares can accelerate protons to several GeV.[21] Figure 1(a) depicts the straggling and range of 10^4 protons for 10, 20, and 68 MeV as well as 1 GeV based on a Monte-Carlo simulation using SRIM[34]. The target is our optimized layer stack comprising glass(quartz)/ITO/PTAA/$Cs_{0.05}MA_{0.17}FA_{0.83}Pb(I_{0.83}Br_{0.17})_3$/$C_{60}$/BCP/Cu. Here, PTAA is poly [bis(4-phenyl)(2,4,6-trimethylphenyl)amine], C_{60} the buckminsterfullerene and BCP bathocuproine. A schematic sketch and a cross-sectional SEM micrograph of a prepared device are depicted in figure 1(b) and (c).

With the nuclear stopping power being proportional to $1/E^2$ already thin substrates provide an effective radiation shield for low energy protons.[35] In our example 1 mm of quartz as substrate is more than sufficient to slow down and stop 10 MeV protons entirely. In contrast, 20 and 68 MeV protons are barely slowed down. As a consequence they release energy throughout the entire device including the perovskite absorber layer. In figure 1(d) the energy loss in $Cs_{0.05}MA_{0.17}FA_{0.83}Pb(I_{0.83}Br_{0.17})_3$ was estimated as a function of the perovskite absorber depth for 20 MeV, 68 MeV and 1GeV.Depicted data is based on the Bragg approximation[36] for compounds and mixtures and presents mean values for $5 \cdot 10^7$ ions simulated in SRIM[34]. In all cases the energy loss is dominated by electronic scattering. This process describes the inelastic scattering of the traversing protons with the atomic electrons. Those are thereby excited and/or ionized. Nuclear scattering on the other hand describes the elastic scattering of the high energetic protons at the target nuclei. Although this process is less frequent, the energy transferred to the recoiling atoms easily exceeds the threshold for a displacement. Consequently, vacancies and interstitials are created.

Simulations depicted in figure 1(d) show that the energy loss to both ionization and recoils decreases by about one order of magnitude for 20 MeV, 68 MeV and 1 GeV respectively Typically, this implies that lower proton energies create about an an order of magnitude more recombination centers. A detailed analysis of the total energy loss to the recoiling nuclei is depicted by the pie chart in figure 1(d). Interestingly, SRIM simulations suggest that the energy loss becomes more and more dominated by the inorganic framework, while increasing the proton energy. Moreover, the average number of primary knock-ons (PKA) decreases from $1.3 \cdot 10^{-6}$ to $3.8 \cdot 10^{-7}$ and $2.7 \cdot 10^{-8}$ $Å^{-1}$ ion^{-1} for 20 MeV, 68 MeV and 1 GeV respectively. . With SRIM being a binary-collision Monte Carlo simulation for amorphous materials, the number of created vacancies and interstitials cannot be estimated precisely. Only detailed molecular dynamic simulations of the involved collision cascades can be used to predict the formation of defects and defect clusters.[37] However, iodine related defects are known as active recombination centers in hybrid perovskites with particularly low formation energies.[38,39] V_I^+ / I_I^- Frenkel pairs for example have a formation energy of ~ 0.3 eV only.[38] Thus, it is highly important to investigate the influence of different incident proton energies on the performance and the properties of perovskite solar cells.

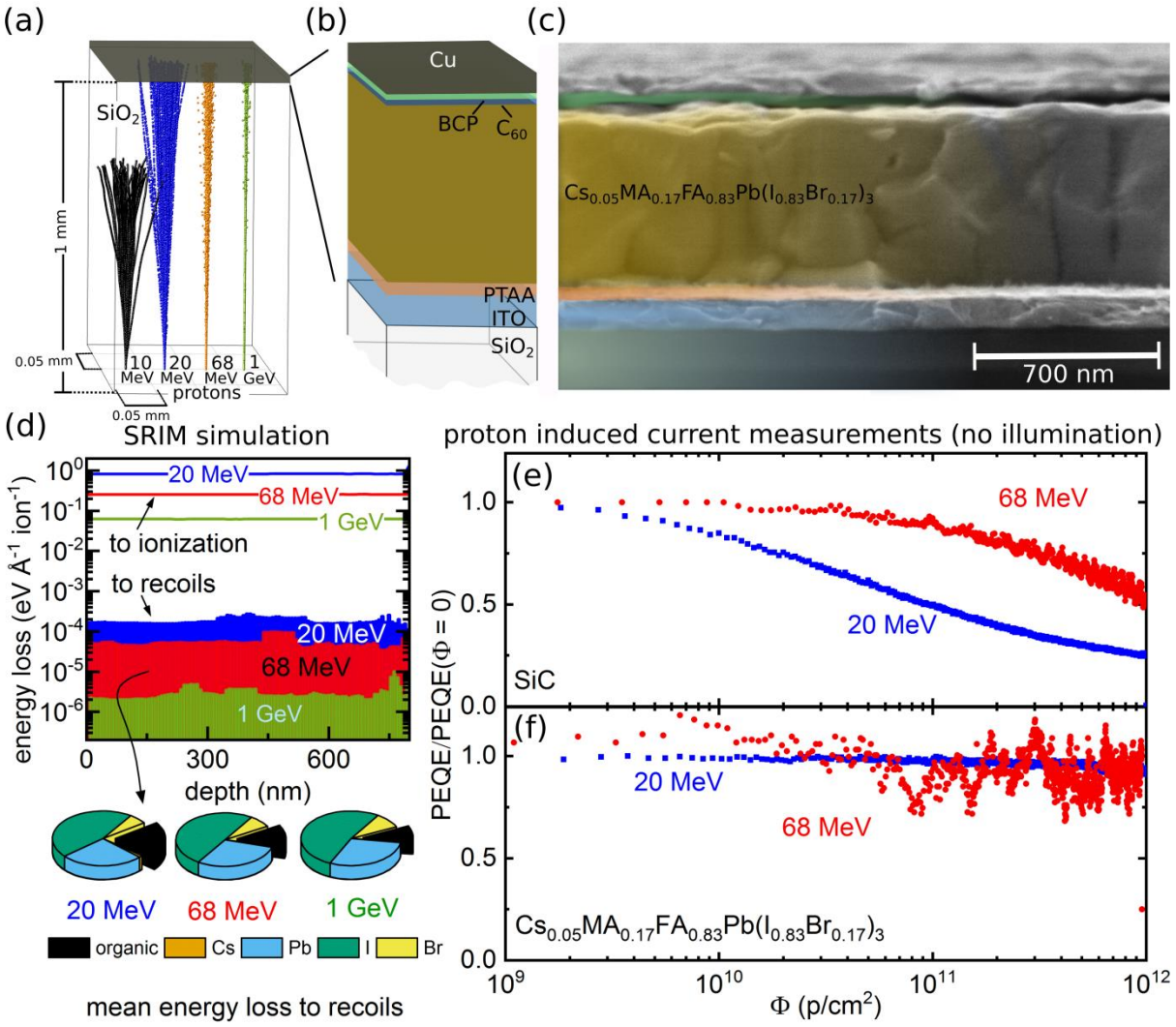

Fig. 1. (a) Simulated straggling of a 10 MeV, 20 MeV, 68 MeV and 1 GeV proton beam in SiO_2 (quartz). (b, c) Sketch and cross-sectional SEM micrograph of the investigated inverted staggered perovskite diodes consisting of the layer stack glass/ITO/PTAA/$Cs_{0.05}MA_{0.17}Fa_{0.83}Pb(I_{0.83}Br_{0.17})_3$/$C_{60}$/BCP/Cu. Devices were encapsulated with a cover glass and epoxy resin (not shown). (d). Energy loss of 20 MeV, 68 MeV and 1 GeV protons to ionization and recoils within the $Cs_{0.05}MA_{0.17}FA_{0.83}Pb(I_{0.83}Br_{0.17})_3$ absorber as a function of the layer depth. Data points represent mean values for $5{\cdot}10^7$ ions simulated using SRIM[34]. Pie charts depict the mean energy loss to Cs, Pb, I, Br and the organic cations. (e, f) *In-situ* measurements of the proton induced current for SiC and $Cs_{0.05}MA_{0.17}Fa_{0.83}Pb(I_{0.83}Br_{0.17})_3$ based diodes under 20 and 68 MeV proton irradiation. Depicted is the relative proton induced external quantum efficiency (PEQE/PEQE(Φ = 0)) as a function of the accumulated proton dose. In case of $Cs_{0.05}MA_{0.17}Fa_{0.83}Pb(I_{0.83}Br_{0.17})_3$ the PEQE(Φ = 0) was $2{\cdot}10^3$ and $5{\cdot}10^2$ for 20 MeV and 68 MeV, respectively.

In-situ measurement of the radiation-induced current

In a semiconductor ionizing radiation leads to the formation of electrons and holes. Both species thermalize down to the respective band edges and can drift in an electric field until being collected via selective contacts. Hence, in any semiconducting diode, ionizing radiation causes a measurable radiation induced current. In our perovskite diodes 20 MeV protons cause a proton induced current (J_p) of 290 nA/cm^2. Considering the employed proton flux (φ) of around 149 pA/cm^2 this translates into a proton induced quantum efficiency (PEQE = J_p / φ) of ~ $2 \cdot 10^3$, meaning that each 20 MeV proton generates more than thousand electron-hole pairs! Exploiting this, could allow novel detectors to measure the flux and energy of high energetic protons.Under 68 MeV proton irradiation the PEQE reduces to $5 \cdot 10^2$, which also manifests as an increase in noise due to the low currents.

During prolonged proton irradiation usually lattice defects are created, which reduce the radiation induced current. The degradation of the PEQE therefore provides a direct and highly sensitive measure of the degradation or the radiation hardness of a material. To illustrate this we investigated the PEQE degradation on a commercially available SiC diode as a function of the accumulated proton dose Φ. SiC is known to possess excellent radiation hardness under high-energy, high-dose proton irradiation.[40] Nevertheless, the data shown in figure 1(e) suggests a considerable degradation of the radiation induced quantum efficiency under proton irradiation. At a dose of 10^{12} p/cm^2 the PEQE decreased by 50 % and 75 % for 20 MeV and 68 MeV, respectively. Our optimized $Cs_{0.05}MA_{0.17}FA_{0.83}Pb(I_{0.83}Br_{0.17})_3$ based diodes in contrast exhibit a PEQE that is extraordinary stable during proton irradiation. The data shown in figure 1(f) demonstrates a degradation of only 7 % at a dose of $\Phi = 10^{12}$ p/cm^2 under both 20 MeV and 68 MeV proton irradiation. This is a strong indication that triple-cation perovskites possess an extraordinary high radiation hardness, making it suitable for application as solar cells in space. But also perovskite based sensors that detect α, β, γ as well as high energetic radiation reliably in harsh environments are possible. After all, the experiment above described the first perovskite based proton detector with a PEQE of ~$2 \cdot 10^3$ and ~$5 \cdot 10^2$ for 20 MeV and 68 MeV protons respectively.

In-situ measurement of the photovoltaic performance

Motivated by this result, we focused on the development of efficient perovskite solar cells that can withstand the harsh radiation environment in space. In this respect it is important that proton irradiation can affect all layers in a solar cell. In transparent crystals and glasses for example, ionization creates free electrons and holes that are trapped in vacancies, impurities and non-bridging oxygen.[41] This creates color-centers that reduce the optical transmission significantly.[26] Consequently, we employed radiation resistant quartz substrates and sputtered a highly transparent ITO layer on top. The optimized layer stack comprised quartz/ITO/PTAA/$Cs_{0.05}MA_{0.17}FA_{0.83}Pb(I_{0.83}Br_{0.17})_3$/$C_{60}$/BCP/Cu, and yielded a power conversion efficiency of 18.8 % under both simulated AM1.5 and AM0 conditions.

To test for the radiation hardness we recorded the *J*-V characteristics *in-situ* under illumination with a halogen lamp and simultaneous proton irradiation. Figure 2(a) depicts mean values of two sets consisting of three devices each that were tested under 20 or 68 MeV proton irradiation. The data demonstrates that the fill factor (FF), the short-circuit current (J_{SC}), the open circuit voltage (V_{OC}) and the efficiency (η) of $Cs_{0.05}MA_{0.17}FA_{0.83}Pb(I_{0.83}Br_{0.17})_3$ based solar cells possess a negligible degradation during irradiation up to an accumulated proton dose of 10^{12} p/cm^2. This result confirms the extraordinary stability of the proton induced current shown before.

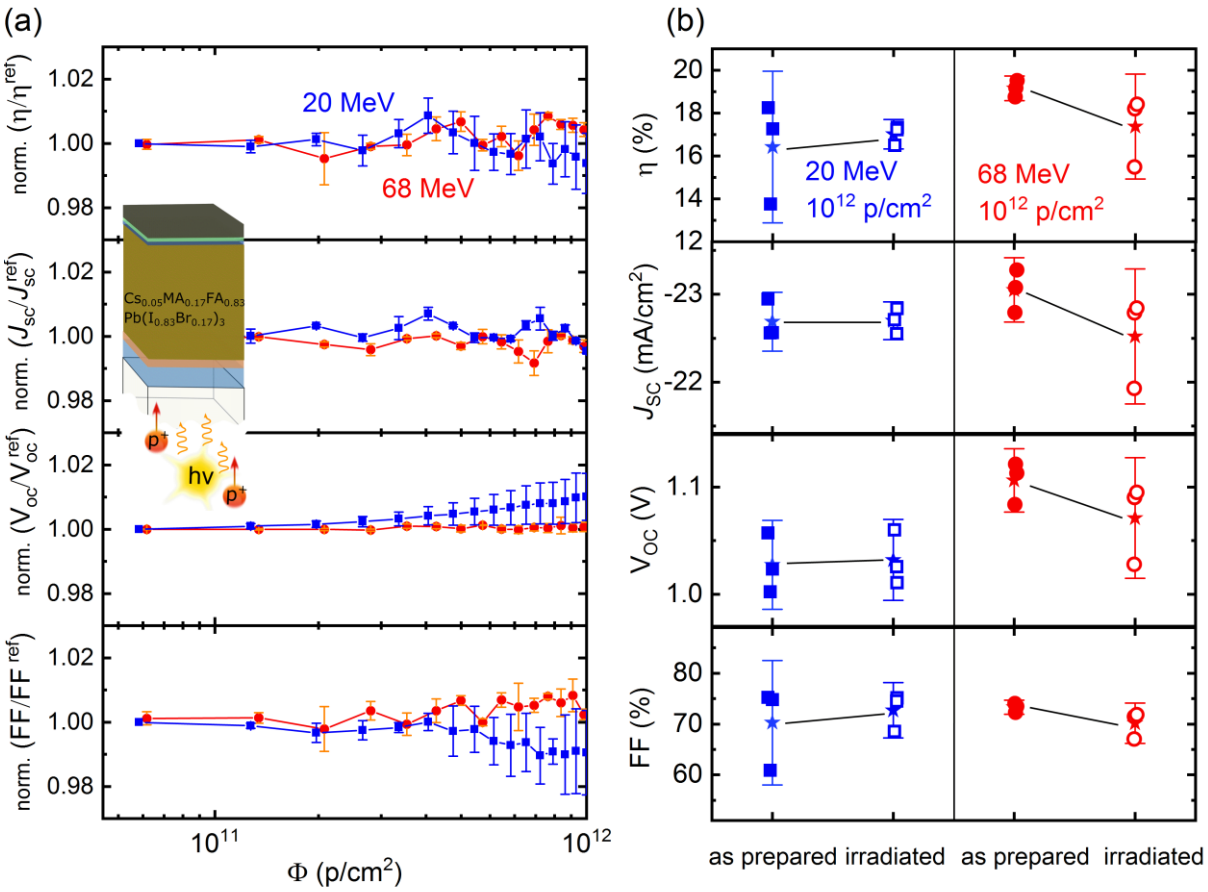

Fig. 2. (a) Evolution of η, J_{sc}, V_{OC}, and FF of a set of $Cs_{0.05}MA_{0.17}FA_{0.83}Pb(I_{0.8}3Br_{0.17})_3$ based solar cells during 20 and 68 MeV proton irradiation as a function of the accumulated proton dose Φ, normalized to non-proton irradiated devices (index ref) that were measured simultaneously. The data was derived from *in-situ* measurements of the *J*-V characteristics during proton irradiation and illumination with light from a halogen lamp. (b) Statistics of η, J_{sc}, V_{OC}, and FF of a set of $Cs_{0.05}MA_{0.17}FA_{0.83}Pb(I_{0.83}Br_{0.17})_3$ based solar cells taken prior to and after proton irradiation with $\Phi = 10^{12}$ p/cm^2. The proton energy was 20 or 68 MeV as indicated. Measurements were performed under simulated AM1.5G conditions. The photovoltaic parameters were derived from reverse measurements.

An identical picture is obtained for *J*-V characteristics recorded after irradiation under a simulated AM1.5 spectrum. As proton irradiation produces radioactive elements in the exposed materials, those measurements were taken 2 weeks later after the radiation decayed to a tolerable level. Figure 2(b) depicts a direct comparison of as prepared and irradiated specimens. Interestingly, the data demonstrates no detrimental effect of 20 MeV proton irradiation. In fact, FF and V_{OC} are even slightly enhanced after irradiation. 68 MeV proton irradiation in contrast causes a very slight decrease in all photovoltaic parameters. The observed reduction of V_{OC}, FF and J_{SC} suggests the formation of a small number of localized defects. This contradicts SRIM simulations shown in figure 1(d) that estimated a higher energy loss in case of 20 MeV proton irradiation. The experimental data, however, clearly demonstrates that 68 MeV proton irradiation

has a stronger impact on the device performance of $Cs_{0.05}MA_{0.17}FA_{0.83}Pb(I_{0.83}Br_{0.17})_3$ based solar cells.

In figure 3 we therefore focus on the effect of 68 MeV irradiation only and depict *J*-V measurements before (solid thick and thin lines) and after irradiation (dashed thick and thin lines) under simulated AM1.5 and AM0 spectra. The measurements were performed from 0 V to V_{OC} (forward scanning, thin lines) and back from V_{OC} to 0 V (reverse scanning direction, thick lines).

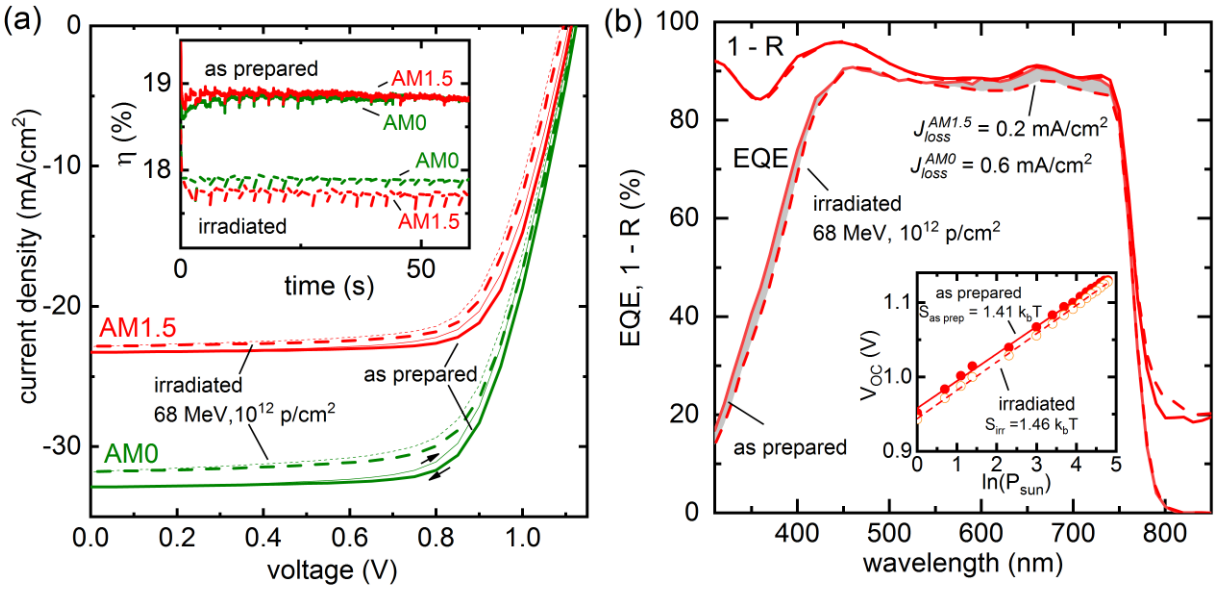

Fig. 3. (a) *J*-V characteristics of $Cs_{0.05}MA_{0.17}FA_{0.83}Pb(I_{0.83}Br_{0.17})_3$ based solar cells taken prior to and after proton irradiation at $\Phi = 10^{12}$ p/cm², E = 68 MeV. Measurements were performed under simulated AM1.5G or AM0 conditions as indicated. The scan direction of the voltage is indicated by arrows. The inset shows the stabilized efficiency from maximum power point tracking. (b) Corresponding external quantum efficiency (EQE) and spectral reflection data. The gray shaded loss in EQE leads to integrated losses of the short circuit current densities as indicated. The inset depicts the V_{OC} as a function of light intensity.

Although there is negligible hysteresis[42] a maximum power point tracking algorithm was employed to determine the stabilized efficiency. Results are shown in the inset of figure 3(a). Under AM0 conditions we determine an efficiency of 18.8 % before and 17.8 % after irradiation with protons at an energy of 68 MeV and a dose of 10^{12} p/cm². This corresponds to a degradation of 1 $\%_{abs}$ and 5 $\%_{rel}$ only. On a satellite relevant orbit it usually takes about 3 years or less to accumulate a dose of 10^{12} p/cm².[21]

To gain further insight into the small loss of J_{SC}, the external quantum efficiency (EQE) and reflection I were probed before and after irradiation as a function of wavelength, figure 3(b).

While the reflection properties remain identical, 68 MeV proton irradiation reduces the EQE in the short and long wavelength range by about 2 $\%_{abs}$. Integrating this reduction leads to a loss in short circuit current densities of about 0.2 mA/cm^2 and 0.6 mA/cm^2 for AM1.5 and AM0 spectra, respectively. These losses correspond well to the reductions observed in the *J*-V characteristics. The inset in figure 3(b) reveals the light intensity dependence of the V_{OC}, which is usually a powerful tool to determine dominant recombination mechanisms.[43] In case of hybrid perovskites, it has recently been shown that the Suns-V_{OC} dependence is indicative for bulk recombination, but not sensitive for surface recombination.[44] Fitting of the Suns-V_{OC} data yields slopes of $S_{as\ prep} = 1.41$ and $S_{irr} = 1.46$. The results indicate an increase of Shockley-Read-Hall (SRH) recombination in the perovskite absorber layer after 68 MeV proton irradiation, corroborating the observed FF, V_{OC} and efficiency losses. It is further realistic to infer a reduction of the charge carrier diffusion length, resulting in a poorer charge collection for short and long wavelengths, as observed in figure 3(b).

3. Characterization of Proton Induced Defects

In-situ measurements shown above have proven an extreme radiation hardness of $Cs_{0.05}MA_{0.17}FA_{0.83}Pb(I_{0.83}Br_{0.17})_3$ based solar cells. Nonetheless, there are some losses that suggest an increased recombination after irradiation with 68 MeV protons. The following provides an in-depth characterization of the effect of proton irradiation on triple cation perovskites. Dark current-voltage (*J*-V) and capacitance-voltage (C-V) characteristics as well as photoluminescence (PL) and V_{OC} decays are analyzed, aiming at a profound understanding of the complex interplay of the proton induced defects.

Dark capacity-voltage and current-voltage characteristics

Ab-initio calculations have suggested that le–d - (V_{Pb}) and methylami–e - (V_{MA}) vacancies are positively charged point defects that are located only 0.05 eV above the valance band maximum (VBM).[45] Consequently, they do not act as recombination centers, but could lead to unintentional p-type doping.[46] $CH_3NH_3PbI_3$ based absorbers, for example, change from an intrinsic to a moderately doped semiconductor during high energetic proton irradiation.[27] To

clarify this, impedance spectra were recorded in the dark and corrected for parasitic effects as described previously.[27]

The frequency independent Maxwell displacement capacitance (C_M) is depicted in figure 4(a).[47,48] In case of intrinsic semiconductors C_M is voltage independent and equals the geometric capacitance between two electrodes $C_M = C_g = \varepsilon\varepsilon_0 A/d$. In case of doped active layers C_M becomes a function of the applied voltage according to the Mott-Schottky model.[49]

$$C_M = A\sqrt{\frac{\epsilon\epsilon_0 qN}{2(V_{bi}-V_{cor})}} \quad (1)$$

Here N denotes the density of uncompensated donors or acceptors, ε the dielectric constant of the PTAA/$Cs_{0.05}MA_{0.17}FA_{0.83}Pb(I_{0.83}Br_{0.17})_3$/$C_{60}$ system, ε_0 the vacuum permittivity, V_{bi} the built-in voltage and $V_{cor} = -V - J \cdot R_s$, the applied bias corrected by the voltage drop over the series resistance. The voltage dependence plotted in figure 4(a) indicates a doped $Cs_{0.05}MA_{0.17}FA_{0.83}Pb(I_{0.83}Br_{0.17})_3$ absorber. The slope of the linear dependence suggests a density of around 10^{15} cm^{-3} uncompensated doping centers.[50] Most importantly, the geometric capacitance C_g, the derived doping density N, as well as the built-in voltage V_{bi} are merely increased after irradiation with 20 or 68 MeV protons. This suggests that the dielectric constant as well as the selective contacts were not affected by 20 or 68 MeV proton irradiation. In addition, shallow defects that act as doping sources were not created.

An interesting situation, however, is observed in figure 4(b) depicting the measured current-voltage (*J*-V) characteristics in dark. The data suggests an significantly improved rectification after proton irradiation. Analysis of the differential resistance $R_{diff} = \Delta V/\Delta J$, figure 4(c), reveals an increase of the parallel resistance by about one order of magnitude after 20 and 68 MeV proton irradiation. This implies significantly lower leakage currents after irradiation. Hence, it appears that the recombination of injected charges via physical shunts in the polycrystalline layer or Shockley-Read-Hall recombination in the bulk is significantly reduced due to proton irradiation. Proton irradiation is indeed an often used technique, for example in the early development of vertical cavity surface emitting lasers (VCSELs), to improve the lateral current confinement and, hence, increase the value of shunt resistances. [51]

In addition to this contradicting result, figure 4(b) also reveals a shift of the *J*-V curve at $J = 0$ by about 150 meV after 68 MeV irradiation (red dashed line). In contrast to all other measurements, this shift depends slightly on the employed scan conditions. Hence, we provide transient data that gives more detailed insight at a later point.

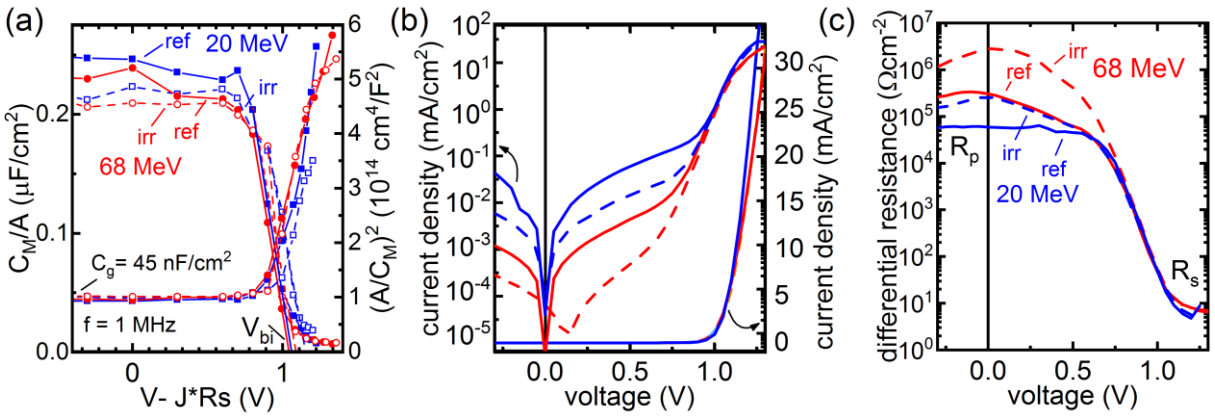

Fig. 4. Electrical properties of proton irradiated $Cs_{0.05}MA_{0.17}FA_{0.83}Pb(I_{0.83}Br_{0.17})_3$ based diodes (dashed lines) compared to identically prepared reference diodes (solid lines). (a) Maxwell displacement capacitance C_M and Mott-Schottky plot as a function of applied voltage at f = 1 MHz. (b) Linear and semi-logarithmic dark *J*-V characteristics. (c) Differential resistance as a function of voltage.

Photoluminescence and V_{OC} decay

To shine light onto the discrepancy between the obviously reduced power conversion efficiency and the apparently better rectification ratio at low bias, photoluminescence (PL) decays were recorded. Time resolved PL has proven to be a reliable and suitable tool to extract the minority-carrier lifetime.[52] For simplicity, we confined our analysis to a double exponential decay (solid lines) and interpret the second, longer decay time as an effective lifetime τ_{eff}. Figure 5(a) depicts PL decays that were recorded on complete device stacks comprising quartz/ITO/PTAA/$Cs_{0.05}MA_{0.17}FA_{0.83}Pb(I_{0.83}Br_{0.17})_3$/$C_{60}$/BCP/Cu. The PL of non irradiated $Cs_{0.05}MA_{0.17}FA_{0.83}Pb(I_{0.83}Br_{0.17})_3$ reference layers on quartz is depicted in figure 5(b). The presence of defective interfaces in the complete device stacks quenches the PL decay compared to the bare films. Indeed, hyperspectral photoluminescence imaging has recently proven that recombination in hybrid perovskites is typically dominated by interfaces between the perovskite and the employed transport layers.[44] Lifetimes extracted for bare non-irradiated reference films reach 135 ns at a excitation fluence of 6 μJ/cm^2, which is well comparable to literature results obtained on high quality perovskite films.[53] As depicted in the inset of figure 5(b), extracted

lifetimes reduce gradually for higher excitations fluences, which is a well-known dependence.[53,54]

Most strikingly, the PL lifetimes double after 68 MeV proton irradiation in both cases, for complete devices and bare perovskite films on quartz. As shown in the inset in figure 5(b), this increased lifetime is only observed for low excitation fluences. A prolongation of the PL decay is usually attributed to a reduced Shockley-Read-Hall (SRH) recombination in the bulk[39,55–58], reduced surface recombination[59–62] or even the deactivation of 'supertraps'[63]. In those cases, however, the increase in lifetimes goes hand in hand with an increase in PL yield. As depicted in Figure 5(c) this is not the case after proton irradiation. In contrast, the data clearly reveals a reduction of PL intensity after proton irradiation. This is typically attributed to an increase of non-radiative recombination. This behavior is consistent with the reduction of the V_{OC} and η after 68 MeV proton irradiation, as depicted in Figure 2(b).

To gain further insight into the dominating recombination mechanisms, we recorded the decay of V_{OC} prior-to and after 68 MeV proton irradiation. Both data sets are depicted as a function of time in figure 5(d). Most strikingly, the V_{OC} of non-irradiated reference devices is found to decay to 0 V within 1 s. The V_{OC} of irradiated devices, in contrast, decays significantly slower. Moreover, after about 1 s a small persistent voltage remains, that decays on a longer timescale. Here we would like to remind, that figure 4(b) revealed a similar effect. There the *J*-V curve after 68 MeV irradiation was shifted at $J = 0$ by about 150 meV. It is likely that this persistent voltage is a result of the prolonged release of charge carriers from radiation induced trap states. This mechanism will be discussed in more detail at a later point.

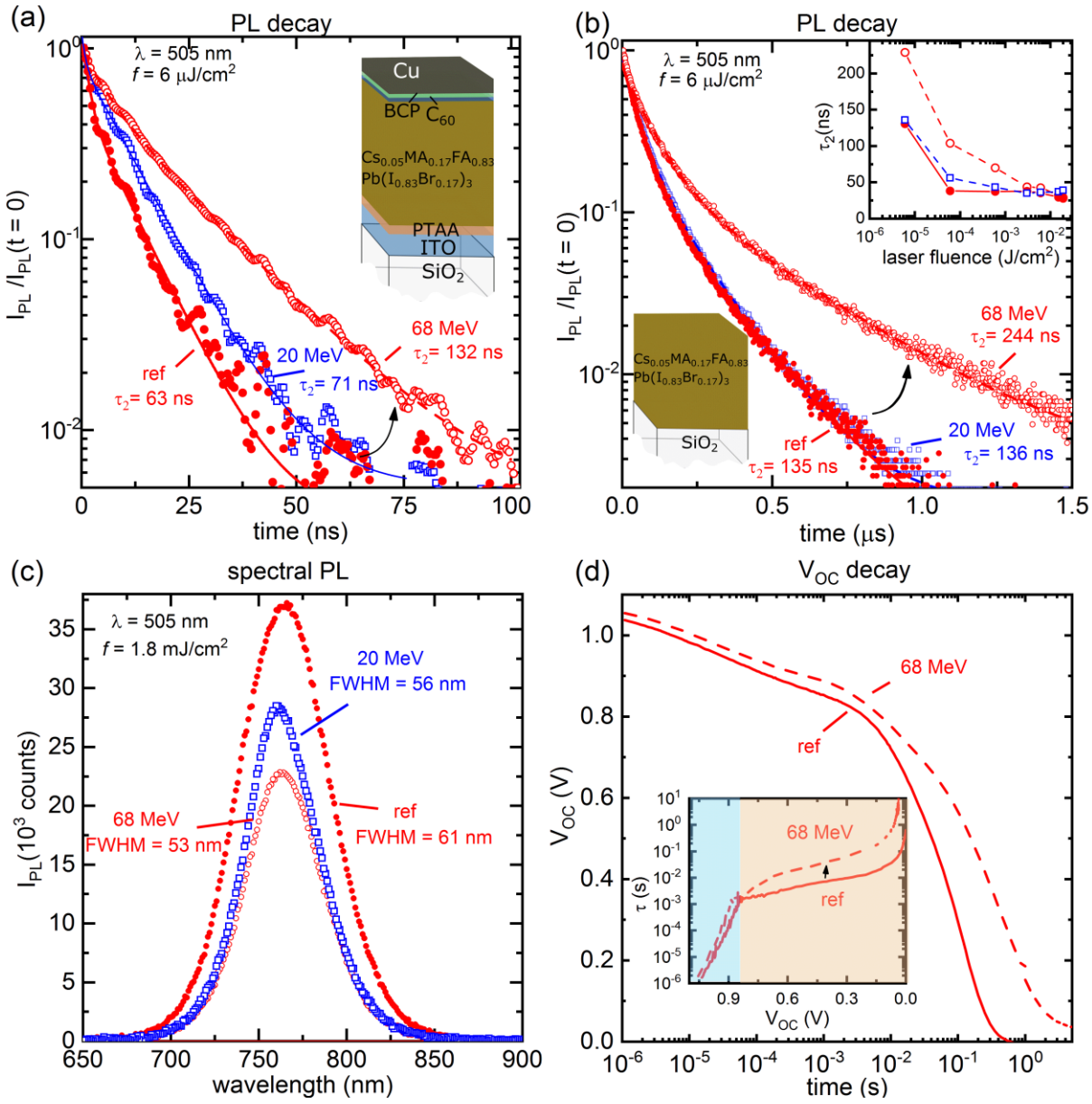

Fig. 5. (a, b) Normalized photoluminescence transients of $Cs_{0.05}MA_{0.17}FA_{0.83}Pb(I_{0.83}Br_{0.17})_3$ based devices and thin-films on quartz. Solid circles represent data obtained on non-irradiated references while open circles refer to proton irradiated specimens. ($\Phi = 10^{12}$ p/cm^2, E = 20 or 68 MeV) Solid lines represent optimized two exponential decays. The inset shows the derived τ_2 as a function of the exciting laser fluencI(c) Photoluminescence spectra of reference and proton irradiated $Cs_{0.05}MA_{0.17}FA_{0.83}Pb(I_{0.83}Br_{0.17})_3$ thin-films on glass. (d) V_{OC} decay of irradiated and reference solar cells. The inset depicts the derived recombination lifetime τ as a function of V_{OC}.

The V_{OC} decay can be used to gain further information on the recombination in the device. Assuming that $n \approx e^{\frac{eV_{OC}}{k_B T}}$ one can define an instant recombination lifetime via $\frac{\mathrm{dn}}{\mathrm{dt}} = \frac{\mathrm{n}}{\tau}$ by equation 2.

$$\tau = -\frac{k_B T}{q}\left(\frac{dV_{oc}}{dt}\right)^{-1} \quad (2)$$

Here k_B is the Boltzmann constant, T the temperature, e the elementary charge and dV_{OC}/dt the derivative of the measured V_{OC} decay over time. Plotting the derived recombination lifetime τ as a function of V_{OC} allows a direct comparison of as prepared and proton irradiated devices at the same charge carrier density n. The data plotted in the inset in figure 5(d) suggests two distinct regimes, in which different recombination mechanisms dominate. At voltages above 0.86 V, τ increases exponentially with decreasing voltage. In this regime, both, the reference and the proton irradiated devices behave very similar. Below 0.86 V, τ rather abruptly deviates from the exponential behaviour and almost saturates. In this regime, proton irradiated devices exhibit an order of magnitude longer recombination lifetime. This suggests a reduced Shockley-Read-Hall recombination although the intensity dependence of Voc suggests a higher contribution from SRH, as presented above.

4. Discussion

Despite the observed remarkable tolerance against high energetic proton irradiation, a quite complex interplay of the radiation induced defects is observed. In the following, insights into the formation of radiation-induced defect states, their nature, as well as their impact on the optoelectronic properties will be deduced. A sound understanding of the formation of radiation-induced defect states is crucial, as any solar cell is exposed to the UV/VIS and NIR part of the electromagnetic spectrum.

Damage mechanisms

J-V measurements under illumination and dark conditions, PL spectra, as well as V_{OC} and PL decay measurements conclusively showed that 68 MeV protons affect the device performance and the recombination mechanism. Only negligible effects were found under 20 MeV proton irradiation. In contrast to this experimental data, SRIM simulations shown in Figure 1(d) predict an order of magnitude higher energy loss associated with electronic scattering and in addition a more dominate reaction with organic nuclei for 20 MeV compared to 68 MeV protons. This indicates that the associated fragmentation of N-H or C-H bonds in the organic cations of $Cs_{0.05}MA_{0.17}FA_{0.83}Pb(I_{0.83}Br_{0.17})_3$ does not cause any active recombination centers. Note that

hydrogen abstraction from C-H bonds is the primary mechanism for radiation induced defects in organic solar cells.[64,65] Also, previous studies identified the fragmentation of N-H bonds in $CH_3NH_3PbI_3$ after prolonged irradiation with light at photon energies larger than 2.7 eV.[66,67] Produced fragments effuse out of the specimen, leaving behind an empty lattice that collapses, or they remain inside the lattice acting as deep recombination centers.[66,67] As no degradation of $Cs_{0.05}MA_{0.17}FA_{0.83}Pb(I_{0.83}Br_{0.17})_3$ is associated with the electronic energy loss we can conclude that fragmented hydrogen does not form localized defects. Instead, displaced hydrogen eventually migrates back quickly, thereby restoring the organic cation in a self-healing mechanism. Indeed, experiments at low temperatures indicated that hydrogen related defect states in $CH_3NH_3PbI_3$ are metastable, thus allowing such a self-healing mechanism.[67] Moreover, self-healing has been observed previously in $CH_3NH_3PbI_3$ after irradiation with light as well as with high energy protons.[26,67,68]

Detailed molecular dynamic simulations of the involved collision cascades and formed defect clusters are required to understand why 68 MeV protons generate more recombination centers that 20 MeV protons do.[37] To provide a first estimate we analyzed the energy loss due to nuclear scattering in SRIM[34], a Monte-Carlo simulation tool based on the binary-collision approximation and an amorphous target. IThe overall energy loss due to nuclear scattering is a factor of four larger for 20 MeV protons compared to 68 MeV. This behavior is expected from the energy dependence of the nuclear scattering cross sections. However, the simulations predict also viewer primary-knock ons, and that the energy loss becomes more and more dominated by the inorganic framework for higher proton energies. It is conceivable that this situation leads to collision cascades that produce more displacements of I or Pb atoms that do not relax back to their lattice position in case of 68 MeV compared to 20 MeV protons. Numerous first principle calculations suggested that iodine related defects are active recombination centers with formation energies below 0.3 eV.[38,39,45] Forming localized recombination centers, those iodine related defects could explain the larger impact of 68 MeV compared to 20 MeV protons irradiation. Strategies that allow to control iodine related defects, e.g. by supplying additional iodine ions[69], hence, could improve the radiation resistance even further.

Tra18etrappingdetrapping at radiation induced defect states

V_{OC} decay and transient PL measurements indicated a drastic change of the recombination mechanism after 68 MeV irradiation. As soon as the quasi-Fermi level splitting (QFLS) drops below ~ 0.86 eV, an order of magnitude longer recombination lifetime is observed analyzing the V_{OC} decay, see e.g. figure 5(d). This result is commonly attributed to a reduced SRH recombination. An important point, however, are results obtained under AM1.5G illumination. There, a slightly reduced device performance is observed. Suns-V_{OC} data performed between 1 and 120 mWcm^{-2} even suggests a slight increased SRH recombination after irradiation, see figure 3(b). In those measurements, the quasi-Fermi level splitting was always above ~ 0.9 V.

Transient PL measurements at low excitation fluences, further, indicate a two-fold increase in lifetime after 68 MeV proton irradiation. This extreme prolongation of the observed lifetimes is a strong indicator for the tra19etrappingdetrapping of charge carriers in a radiation induced trap state. Minority charge carrier trapping is known to have a strong impact on the charge carrier dynamics. Anomalously high apparent lifetimes are known from poor-quality single-crystal and multi-crystalline silicon.[70,71] Already in the mid-1950'ies Hornbeck and Haynes[71] described this phenomena both qualitatively and quantitatively.

To corroborate19etrappingdetrapping of minority charge carriers from radiation induced defects causes prolonged apparent lifetimes in $Cs_{0.05}MA_{0.17}FA_{0.83}Pb(I_{0.83}Br_{0.17})_3$, we simulated the PL decay. Our model, follows Hornbeck and Haynes[71] but includes Auger- and radiative recombination as well as the tra19etrappingdetrapping of minority carriers into and from radiation induced trap states. The involved processes are illustrated in figure 6. Following a variety of reports[54,72,73], electrons were assumed as minority charge carriers. The same formalism, however, holds for a minority of holes as well. Our kinetic model is, hence, well described by the coupled differential equations for electrons n_e, holes n_h and populated electron traps n_t, with N_{trap} being the total available trap density.

$$\frac{\mathrm{d}n_e^i}{\mathrm{dt}} = -\underbrace{\gamma_{Auger} \cdot {n_e^i}^2 \cdot n_h^i}_{Auger} - \underbrace{\mathrm{k}_{rad} \cdot n_e^i \cdot n_h^i}_{radia-ive} - \underbrace{k_{trap} \cdot n_e^i \cdot N_{trap} \cdot \left(1 - \frac{n_{trap}^i}{N_{trap}}\right)}_{trapping} + \underbrace{k_{detrap} \cdot n_{trap}^i \cdot N_{trap}}_{detrapping} \quad (3)$$

$$\frac{\mathrm{d}n_{h\mathrm{h}}^i}{\mathrm{dt}} = -\underbrace{\gamma_{Auger} \cdot n_e^i \cdot {n_h^i}^2}_{Auger} - \underbrace{\mathrm{k}_{rad} \cdot n_e^i \cdot n_h^i}_{radiative} \quad (4)$$

$$\frac{\mathrm{d}n_{trap}^{i}}{\mathrm{dt}} = \underbrace{k_{trap} \cdot n_e^i \cdot N_{trap} \cdot \left(1 - \frac{n_{trap}^{i}}{N_{trap}}\right)}_{trapping} - \underbrace{k_{detrap} \cdot n_{trap}^{i} \cdot N_{trap}}_{detrapping} \quad (5)$$

This set of coupled differential equations was solved numerically and iteratively optimized to the experimental data employing a least square algorithm. As shown in figure 6, black dotted line, the PL decay of non-irradiated reference films is well described without radiation induced trap states ($N_{trap} = 0$ cm^{-3}). Optimized Auger coefficients of $\gamma_{Auger} = 2.4 \cdot 10^{-26}$ cm^6/s and radiative recombination coefficients of $k_{rad} = 1.0 \cdot 10^{-11}$ cm^6/s are in good agreement with previously published values.[54,74] Deriving these values accurately requires to consider the doping concentration.[54] According to C-V measurements shown in figure 4(a) the doping concentration of the investigated $Cs_{0.05}MA_{0.17}FA_{0.83}Pb(I_{0.83}Br_{0.17})_3$ films is about 10^{15} cm^{-3} for proton irradiated as well as reference specimens. In a second step, the PL decay of the proton irradiated specimen was modelled including the tra20etrappingdetrapping into and from radiation induced trap states, while fixing the γ_{Auger} and k_{rad} constants. With a trap density of $N_{trap} = 9 \cdot 10^{-13}$ cm^{-3} and a20etrappingdetrapping ratio of $k_{trap}/k_{detrap} = 0.34$ the prolonged PL decay is well modelled. In fact, the simulated PL decay shown as black solid line in Figure 6 accurately captures the entire range of the experimentally determined PL decay after 68 MeV proton irradiation. Cons20etrappingdetrapping of minority charge carriers causes the prolonged PL decay and slower V_{OC} decays observed after 68 MeV proton irradiation. Considering the nuclear scattering, it is likely that these trap states are related to a displaced iodine atom located at an interstitial site. Time-domain *ab-initio* studies of pristine $CH_3NH_3PbI_3$ suggested that interstitial iodine creates sub-gap states capable of trapping both electrons and holes.[75] Moreover, recent first principle calculations by Meggiolaro et al. [39] highlighted the role of interstitial iodine in $CH_3NH_3PbI_3$ due to its low formation energy and various charge states.

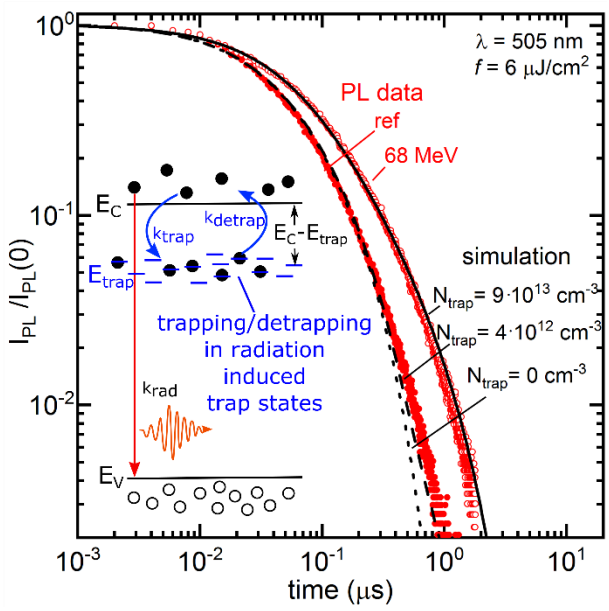

Fig. 6. Simulated and experimental photoluminescence decay of $Cs_{0.05}MA_{0.17}FA_{0.83}Pb(I_{0.83}Br_{0.17})_3$ thin-films prior to and after proton irradiation ($\Phi = 10^{12}$ p/cm^2, E = 68 MeV). Black dotted, dashed and solid lines refer to simulations with a trap density of $N_t = 0$, $4\cdot10^{12}$ and $9\cdot10^{13}$ cm^{-3}, respectively.

γ_{Auger}	k_{rad}	k_{trap}	k_{detrap}	k_{trap}/k_{detrap}	E_C-E_{trap}
$2.4\cdot10^{-26}$ cm^6/s	$1.0\cdot10^{-11}$ cm^3/s	$2.9\cdot10^{-8}$ cm^3/s	$8.5\cdot10^{-9}$ cm^3/s	3.4	0.31 eV

Table. 1. Optimized parameters employed in the kinetic model.

In thermal equilibrium, the energetic depth of the involved trap states can be estimated from the tra21etrappingdetrapping rates via [71,76]

$$E_C - E_{trap} = k_B T \cdot \ln\left(\frac{N_C}{N_t} \cdot \frac{k_{trap}}{k_{detrap}}\right). \quad (6)$$

Assuming an electron mass of 0.35[77] yields an effective density of states in the conduction band of $N_C = 2 \cdot \left[\frac{2\pi \cdot m_e \cdot kT}{h^2}\right]^{\frac{3}{2}} = 5.2\cdot10^{18}$ cm^{-3}.[50] Hence this suggests a trap state located ~ 0.31 eV within the band gap. This value may also represent an average position from more than one trap level present after proton irradiation. Most importantly, however, the derived trap depth is sufficiently deep to explain the observed demarcation threshold at a QFLS ~ 0.86 eV, separating two regimes with distinct recombination mechanisms. To illustrate this we can estimate the QFLS just extending into the trap states via: $E_g - 2 \cdot (E_C - E_{trap}) - \Delta E_{interface} \approx 0.9\ eV$, corresponding well to the experimentally observed threshold of ~ 0.86 V. Hereby, additional losses at the

interfaces with PTAA and C_{60} of at least $\Delta E_{interface} \sim 0.089$ V[44] have been considered. Moreover, slow detrapping of minority charge carriers from traps states located ~ 0.31 eV within the band gap can explain the persistent voltage observed after excitation or during *J*-V measurements, see figure 4(b) and 5(d). Integrating the measured PL decay depicted in figure 6 yields values of $9 \cdot 10^{-9}$ counts·s and $9 \cdot 10^{-9}$ counts·s for reference and proton irradiated specimens, respectively. This implies that the release of trapped minority carriers is highly efficient. Consequently, the solar cell performance under continuous AM1.5G or AM0 operating conditions is barely affected.

Interestingly, simulations depicted in figure 6 suggest that as prepared specimens already contain a small number of these trap states. The associated trapping and detrapping of minority charge carriers of course induces fluctuations in the charge carrier density becoming a main noise source.[78] Noise measurements by Landi et al.[79] have recently demonstrated that trapping/detrapping occurs in $CH_3NH_3PbI_3$ based solar cells. Moreover, Chirvony et al.[80,81], recently described an extremely delayed photoluminescence in $CH_3NH_3PbBr_3$ nanocrystals, again associated with slow release of trapped minority charge carriers.[80,81]

Knowing that efficient trapping/detrapping of minority carriers can prolong observed PL decays in hybrid perovskites significantly, extreme care must be taken when interpreting transient measurements. Additional direct measurements of e.g. the diffusion length via the Goodman method[82,83] are recommended to verify improved bulk properties. The proposed trapping/detrapping of minority charge carriers may also occur at light-induced defect states. Our understandings, therefore, may provide a new perspective on light-induced phenomena. The slow release of trapped charge carriers from defects present in as-prepared perovskite films and single crystals may also contribute to the vastly differing lifetimes described in literature.[84]

3. Conclusion

In conclusion, we employed a variety of *in-situ* and *ex-situ* measurements to demonstrate, for the first time, that perovskite solar cells made from $Cs_{0.05}MA_{0.17}FA_{0.83}Pb(I_{0.83}Br_{0.17})_3$ are radiation hard and possess negligible degradation under high-energy, high-dose proton irradiation. Analyzing the radiation induced current during irradiation with 68 MeV and 20 MeV protons we found that $Cs_{0.05}MA_{0.17}FA_{0.83}Pb(I_{0.83}Br_{0.17})_3$ even exceeds the radiation hardness of SiC, which is often proposed to possess an excellent radiation hardness. Our optimized $Cs_{0.05}MA_{0.17}FA_{z0.83}Pb(I_{0.83}Br_{0.17})_3$ based space solar cells reach efficiencies of 18.8 % under simulated AM0 illumination and maintain 95 % of their initial efficiency even after irradiation with protons at an energy of 68 MeV and a total dose of 10^{12} p/cm^2, which is an equivalent to around 3 years in space. An even smaller impact was found under 20 MeV proton irradiation, although the electronic energy loss of 20 MeV protons is about 1 order of magnitude higher compared to 68 MeV protons. This result emphasizes the role of iodine related defect states. Despite the minor impact on device performance the recombination kinetics change profoundly under low excitation levels. After 68 MeV proton irradiation, a significant slower decay of the open circuit voltage and photoluminescence intensity is observed below a quasi-Fermi level splitting of 0.86 V. A kinetic model able to describe the PL decay accurately, establishes the prolonged release of trapped minority charge carriers from radiation induced trap states. Although located ~ 0.3 eV within the band gap, these radiation induced trap states release trapped minority carriers efficiently. Consequently the recombination kinetics under normal, high excitation conditions are barely effected, explaining the observed radiation hardness.

4. Experimental

Preparation of Triple-Cation Perovskite Solar Cells: The fabricated perovskite solar cells were based on an inverted planar (p-i-n) structure and our optimized layer stack comprised quartz/ITO/PTAA/$Cs_{0.05}MA_{0.17}FA_{0.83}Pb(I_{0.83}Br_{0.17})_3$/$C_{60}$/BCP/Cu. First, quartz substrates were cleaned using acetone, detergent/H_2O, H_2O, isopropyl alcohol, and ozone. Then, a 50 nm thick ITO layer was RF-sputtered through a shadow mask from a ceramic target. The oxygen content in the Ar/O_2 sputter gas mixture was 0.1% and the deposited layers were annealed in air at 200°C for 5 min. Prepared substrates were subsequently transferred to an inert environment and a thin layer of the hole transport material PTAA was deposited from a 2 mg/ml solution in toluene by spin-coating at 4000 rpm for 30 s. After an anneal for 10 min at 100 °C the perovskite $Cs_{0.05}MA_{0.17}FA_{0.83}Pb(I_{0.83}Br_{0.17})_3$ was prepared. Therefore a typical triple cation process based on a one-step spin coating process at 4000 rpm for 35 s and a 400 µl ethyl acetate anti-solvent drop after 25 s was utilized.[1,85] After annealing at 100 °C for 1 h, 23 nm of C_{60} and 8 nm of BCP were thermally evaporated at a rate of 0.15 Å/s and 0.2 Å/s respectively. Lastly, 100 nm of Cu were thermally evaporated through a shadow mask. This defined the active device area to 0.20 s ± 0.1 cm^2, measured under an optical microscope. The fabricated solar cells were then encapsulated under inert atmosphere using a cover glass and epoxy resin.

Proton Irradiation: For the irradiation experiments protons were accelerated to an energy of 68 ± 1 MeV using the tandetron-cyclotron combination of the Helmholtz-Zentrum Berlin. [86,87] To achieve a homogeneous irradiation over an area of 3.0 cm^2 a thin scattering foil was used. Thicker aluminum plates were used to provide (10 ± 3) and (20 ± 3) MeV protons. In all cases, the beam intensity was monitored online utilizing a transmission ionization chamber.

In-situ measurements: In-situ measurements of the radiation-induced currents were recorded at V = 0 V during proton irradiation under dark conditions. *In-situ* measurements of the photovoltaic parameters were recorded during simultaneous proton irradiation and illumination from a halogen lamp. (P = 25 mW/cm^2). Therefore, current-voltage scans were recorded automatically in reverse direction using a Keithley 2400.

Characterization: AM1.5G and AM0 spectra were simulated using a Wavelabs Sinus 70 AAA LED sun simulator, adjusted to 100 or 135 mW/cm^2 respectively by measuring the short circuit current of a calibrated silicon solar cell (Fraunhofer ISE). The spectral irradiance of the

mimicked spectra were measured and the mismatch factors between 300 and 900 nm in 100 nm intervals amounted to 0.56, 0.95, 0.93, 0.94, 1.04, 0.92 for AM0 and 0.56, 0.93, 0.91, 0.93, 0.94, 0.93 for AM1.5G spectra respectively. Current-voltage scans were performed in forward and reverse direction with voltage sweep of 85 mV/s. Hysteresis was negligible in case of both as prepared and irradiated devices. Hence, the maximum power points for forward and reverse scan directions were identical. Additionally, we tracked the maximum power point (MPP) using homemade feedback software. In all cases, the temperature amounted to 25°C. In some cases, shadow masks (A = 0.0961 cm^2) were used to avoid any underestimation of the active area. Different light intensities were obtained by modulating the LED intensity and additional neutral filters. External quantum efficiencies (EQE) were measured without bias voltage or bias illumination. From the measured EQE spectra a current density of 21.3 mA/cm^2 was estimated. This value is about 7% lower than the J_{SC} obtained under AM1.5G illumination and suggest some spectral mismatch. Photoluminescence spectra were recorded after excitation from a pulsed dye laser with a wavelength of λ_{exc} = 505 nm. The laser fluence amounted to 6 $\mu J/cm^2$ for transient measurements and to 12 mJ/cm^2 in case of spectral dependent measurements. Impedance measurements were recorded in the dark by applying a DC potential overlaid by an AC perturbation of 10 mV. The applied DC potential was varied between -1.2 V and 1.5 V, while the frequency of the AC perturbation was varied between 20 Hz and 1 MHz. V_{OC} decay measurements were recorded after excitation from a fast switching 100 mW/cm^2, 465 – 470 nm LED light source. Most notably, the switch-off time of the light source was below 30 ns. V_{OC} decays were detected with a high impedance buffer of 5 GΩ and a digital oscilloscope.

Simulations: STRIM simulations were performed on $5 \cdot 10^7$ ions simulated using SRIM[34]. Employed densities and thicknesses were: ρ_{quartz} =1.72 g/cm^3 d_{quartz} =$1 \cdot 10^7$ Å, ρ_{ITO} =7.2 g/cm^3 d_{quartz} =$1 \cdot 10^3$ Å, ρ_{PTAA} =1.2 g/cm^3 d_{PTAA} =$5 \cdot 10^1$ Å, $\rho_{perovskite}$ =4.59 g/cm^3 $d_{perovskite}$ =$8 \cdot 10^3$ Å, ρ_{C60} =1.65 g/cm^3 d_{C60} =$5 \cdot 10^1$ Å, ρ_{Cu} =8.92 g/cm^3 d_{Cu} =$1 \cdot 10^3$ Å. Kinetic simulations of the PL decay were performed numerically in python[88].

Acknowledgments

The authors would like to express their deepest gratitude to Prof. B. Rech who encouraged us to test hybrid perovskites for their radiation hardness. Prof. B. Rech further supported the entire project with advice & paved the way for the experimental realization. Moreover, the authors are grateful to Dr. J. C. Stang for sputtering ITO and C. Klimm for taking

SEM micrographs. F.L. further thanks H. Näsström, Dr. A. Merdasa, and especially Dr. V. V. Brus and Dr. O. Shargaieva for useful discussions. Moreover, F.L would like to thank Dr. S. Stranks and his group for all their support as well as inspiring discussions. M.J and S.A. acknowledge financial support from the German Federal Ministry of Education and Research (BMBF) via program “Materialforschung für die Energiewende” (grant no. 03SF0540). F.L. acknowledges financial support from the Alexander von Humboldt Foundation via the Feodor Lynen program.

References

[1] M. Saliba, T. Matsui, J.-Y. Seo, K. Domanski, J.-P. Correa-Baena, M. K. Nazeeruddin, S. M. Zakeeruddin, W. Tress, A. Abate, A. Hagfeldt, M. Grätzel, *Energy Environ. Sci.* **2016**, *9*, 1989.

[2] J.-W. Lee, D.-H. Kim, H.-S. Kim, S.-W. Seo, S. M. Cho, N.-G. Park, *Adv. Energy Mater.* **2015**, *5*, 1501310.

[3] M. Saliba, T. Matsui, K. Domanski, J.-Y. Seo, A. Ummadisingu, S. M. Zakeeruddin, J.-P. Correa-Baena, W. R. Tress, A. Abate, A. Hagfeldt, M. Grätzel, *Science* **2016**, *354*, 206.

[4] N. Pellet, P. Gao, G. Gregori, T.-Y. Yang, M. K. Nazeeruddin, J. Maier, M. Grätzel, *Angew. Chemie Int. Ed.* **2014**, *53*, 3151.

[5] F. Lang, O. Shargaieva, V. V. Brus, H. C. Neitzert, J. Rappich, N. H. Nickel, *Adv. Mater.* **2018**, *30*, 1702905.

[6] W. Rehman, D. P. McMeekin, J. B. Patel, R. L. Milot, M. B. Johnston, H. J. Snaith, L. M. Herz, *Energy Environ. Sci.* **2017**, *10*, 361.

[7] N. J. Jeon, H. Na, E. H. Jung, T. Y. Yang, Y. G. Lee, G. Kim, H. W. Shin, S. Il Seok, J. Lee, J. Seo, *Nat. Energy* **2018**, *3*, 682.

[8] NREL, "Research Cell Efficiency Records," can be found under http://www.nrel.gov/ncpv/images/efficiency_chart.jpg, **2018**.

[9] E. L. Unger, L. Kegelmann, K. Suchan, D. Sörell, L. Korte, S. Albrecht, *J. Mater. Chem. A* **2017**, *5*, 11401.

[10] T. Leijtens, R. Prasanna, K. A. Bush, G. E. Eperon, J. A. Raiford, A. Gold-Parker, E. J. Wolf, S. A. Swifter, C. C. Boyd, H.-P. Wang, M. F. Toney, S. F. Bent, M. D. McGehee, *Sustain. Energy Fuels* **2018**, *2*, 2450.

[11] M. Jošt, E. Köhnen, A. B. Morales-Vilches, B. Lipovšek, K. Jäger, B. Macco, A. Al-Ashouri, J. Krč, L. Korte, B. Rech, R. Schlatmann, M. Topič, B. Stannowski, S. Albrecht, *Energy Environ. Sci.* **2018**, *11*, 3511.

[12] Q. Han, Y. Hsieh, L. Meng, J. Wu, P. Sun, E. Yao, S. Chang, S. Bae, T. Kato, V. Bermudez, Y. Yang, *Science* **2018**, *361*, 904.

[13] A. F. Hepp, J. S. Mcnatt, S. G. Bailey, S. Sun, C. E. Bonner, D. Rauh, *IEEE A&E Syst.* **2008**.

[14] B. Hoang, S. White, B. Spence, S. Kiefer, in *2016 IEEE Aerosp. Conf.*, IEEE, **2016**, pp. 1–12.

[15] J. Banik, S. Kiefer, M. LaPointe, P. LaCorte, in *2018 IEEE Aerosp. Conf.*, IEEE, **2018**, pp. 1–9.

[16] P. A. Jones, B. R. Spence, in *1998 IEEE Aerosp. Conf. Proc. (Cat. No.98TH8339)*, IEEE, **n.d.**, pp. 141–152.

[17] M. Kaltenbrunner, G. Adam, E. D. Głowacki, M. Drack, R. Schwödiauer, L. Leonat, D. H.

Apaydin, H. Groiss, M. C. Scharber, M. S. White, N. S. Sariciftci, S. Bauer, *Nat. Mater.* **2015**, *14*, 1032.

[18] K. Otte, L. Makhova, A. Braun, I. Konovalov, *Thin Solid Films* **2006**, *511–512*, 613.

[19] C. R. Brown, G. E. Eperon, V. R. Whiteside, I. R. Sellers, *ACS Appl. Energy Mater.* **2018**, *2*, 814.

[20] E. J. Daly, G. Drolshagen, A. Hilgers, H. D. R. Evans, *Environ. Model. Space-based Appl. Symp. Proc.* **1996**, 15.

[21] T. Markvart, *J. Mater. Sci. Mater. Electron.* **1990**, *1*, 1.

[22] A. Jasenek, U. Rau, K. Weinert, H. W. Schock, J. H. Werner, *Photovolt. Energy Conversion, 2003. Proc. 3rd World Conf.* **2003**, *1*, 593.

[23] R. J. Walters, H. . Cotal, S. R. Messenger, E. A. Burke, S. J. Wojtczuk, H. B. Serreze, P. R. Sharps, M. L. Timmons, P. Iles, Y. C. M. Yeh, *Sol. Energy Mater. Sol. Cells* **1998**, *50*, 305.

[24] S. Park, J. C. Bourgoin, H. Sim, C. Baur, V. Khorenko, O. Cavani, J. Bourcois, S. Picard, B. Boizot, *Prog. Photovoltaics Res. Appl.* **2018**, *26*, 778.

[25] H. C. Neitzert, P. Spinillo, S. Bellone, G. D. Licciardi, M. Tucci, F. Roca, L. Gialanella, M. Romano, *Sol. Energy Mater. Sol. Cells* **2004**, *83*, 435.

[26] F. Lang, N. H. Nickel, J. Bundesmann, S. Seidel, A. Denker, S. Albrecht, V. V. Brus, J. Rappich, B. Rech, G. Landi, H. C. Neitzert, *Adv. Mater.* **2016**, *28*, 8726.

[27] V. V Brus, F. Lang, J. Bundesmann, S. Seidel, A. Denker, B. Rech, G. Landi, H. C. Neitzert, J. Rappich, N. H. Nickel, *Adv. Electron. Mater.* **2017**, *3*, 1600438.

[28] Y. Miyazawa, M. Ikegami, H.-W. Chen, T. Ohshima, M. Imaizumi, K. Hirose, T. Miyasaka, *iScience* **2018**, *2*, 148.

[29] Y. Miyazawa, M. Ikegami, T. Miyasaka, T. Ohshima, M. Imaizumi, K. Hirose, in *2015 IEEE 42nd Photovolt. Spec. Conf.*, IEEE, **2015**, p. 1.

[30] C. G. Bischak, C. L. Hetherington, H. Wu, S. Aloni, D. F. Ogletree, D. T. Limmer, N. S. Ginsberg, *Nano Lett.* **2017**, *17*, 1028.

[31] S. Yang, Z. Xu, S. Xue, P. Kandlakunta, L. Cao, J. Huang, *Adv. Mater.* **2018**, *1805547*, 1805547.

[32] S. Yakunin, M. Sytnyk, D. Kriegner, S. Shrestha, M. Richter, G. J. Matt, H. Azimi, C. J. Brabec, J. Stangl, M. V. Kovalenko, W. Heiss, *Nat. Photonics* **2015**, *9*, 444.

[33] H. Wei, Y. Fang, P. Mulligan, W. Chuirazzi, H.-H. Fang, C. Wang, B. R. Ecker, Y. Gao, M. A. Loi, L. Cao, J. Huang, *Nat. Photonics* **2016**, *10*, 333.

[34] J. F. Ziegler, M. D. D. Ziegler, J. P. P. Biersack, *Nucl. Instruments Methods Phys. Res. Sect. B Beam Interact. with Mater. Atoms* **2010**, *268*, 1818.

[35] J. R. Tesmer, M. A. Nastasi, M. Tesmer, J R;Nastasi, *Handbook of Modern Ion Beam*

Analysis, Materials Research Society, Pittsburgh, Pennsilvania, **1995**.

[36] W. H. Bragg, R. Kleeman, *London, Edinburgh, Dublin Philos. Mag. J. Sci.* **1905**, *10*, 318.

[37] X. Xiang, T. Jinjun, *China Foundry* **2010**, *7*, 253.

[38] E. Mosconi, D. Meggiolaro, H. J. Snaith, S. D. Stranks, F. De Angelis, *Energy Environ. Sci.* **2016**, *9*, 3180.

[39] D. Meggiolaro, S. Motti, E. Mosconi, A. barker, J. Ball, C. A. R. Perini, F. Deschler, A. Petrozza, F. De Angelis, *Energy Environ. Sci.* **2018**, *11*, 702.

[40] Z. Luo, T. Chen, A. C. Ahyi, A. K. Sutton, B. M. Haugerud, J. D. Cressler, D. C. Sheridan, J. R. Williams, P. W. Marshall, R. A. Reed, *IEEE Trans. Nucl. Sci.* **2004**, *51*, 3748.

[41] M. F. Bartusiak, J. Becher, *Appl. Opt.* **1979**, *18*, 3342.

[42] E. L. Unger, E. T. Hoke, C. D. Bailie, W. H. Nguyen, A. R. Bowring, T. Heumüller, M. G. Christoforo, M. D. McGehee, *Energy Environ. Sci.* **2014**, *7*, 3690.

[43] S. R. Cowan, A. Roy, A. J. Heeger, *Phys. Rev. B* **2010**, *82*, 245207.

[44] M. Stolterfoht, C. M. Wolff, J. A. Márquez, S. Zhang, C. J. Hages, D. Rothhardt, S. Albrecht, P. L. Burn, P. Meredith, T. Unold, D. Neher, *Nat. Energy* **2018**, *3*, 847.

[45] W.-J. Yin, T. Shi, Y. Yan, *Appl. Phys. Lett.* **2014**, *104*, 063903.

[46] J. Kim, S. H. Lee, J. H. Lee, K. H. Hong, *J. Phys. Chem. Lett.* **2014**, *5*, 1312.

[47] R. S. Sanchez, V. Gonzalez-Pedro, J. Lee, N. Park, Y. S. Kang, I. Mora-Sero, J. Bisquert, *J. Phys. Chem. Lett.* **2014**, *5*, 2357.

[48] J. Bisquert, L. Bertoluzzi, I. Mora-Sero, G. Garcia-Belmonte, *J. Phys. Chem. C* **2014**, *118*, 18983.

[49] O. Almora, C. Aranda, E. Mas-Marzá, G. Garcia-Belmonte, *Appl. Phys. Lett.* **2016**, *109*, 173903.

[50] S. M. Sze, *Physics of Semiconductor Devices*, John Wiley & Sons, Inc, New York, **1981**.

[51] Y. Aoki, M. Miyamoto, H. Naito, A. Higuchi, K. Torii, T. Nagakura, N. Kageyama, H. Aoshima, T. Morita, J. Maeda, H. Yoshida, *IEEE J. Quantum Electron.* **2014**, *50*, 510.

[52] R. K. Ahrenkiel, *Solid State Electron.* **1992**, *35*, 239.

[53] M. Abdi-Jalebi, Z. Andaji-Garmaroudi, S. Cacovich, C. Stavrakas, B. Philippe, J. M. Richter, M. Alsari, E. P. Booker, E. M. Hutter, A. J. Pearson, S. Lilliu, T. J. Savenije, H. Rensmo, G. Divitini, C. Ducati, R. H. Friend, S. D. Stranks, *Nature* **2018**, *555*, 497.

[54] F. Staub, H. Hempel, J.-C. Hebig, J. Mock, U. W. Paetzold, U. Rau, T. Unold, T. Kirchartz, *Phys. Rev. Appl.* **2016**, *6*, 044017.

[55] D. J. Kubicki, D. Prochowicz, A. Hofstetter, M. Saski, P. Yadav, D. Bi, N. Pellet, J. Lewiński,

S. M. Zakeeruddin, M. Grätzel, L. Emsley, *J. Am. Chem. Soc.* **2018**, *140*, 3345.

[56] C. Wehrenfennig, G. E. Eperon, M. B. Johnston, H. J. Snaith, L. M. Herz, *Adv. Mater.* **2014**, *26*, 1584.

[57] Y. Fu, F. Meng, M. B. Rowley, B. J. Thompson, M. J. Shearer, D. Ma, R. J. Hamers, J. C. Wright, S. Jin, *J. Am. Chem. Soc.* **2015**, *137*, 5810.

[58] Y. Liu, Y. Zhang, Z. Yang, D. Yang, X. Ren, L. Pang, S. F. Liu, *Adv. Mater.* **2016**, *28*, 9204.

[59] A. Abate, M. Saliba, D. J. Hollman, S. D. Stranks, K. Wojciechowski, R. Avolio, G. Grancini, A. Petrozza, H. J. Snaith, *Nano Lett.* **2014**, *14*, 3247.

[60] R. Brenes, D. Guo, A. Osherov, N. K. Noel, C. Eames, E. M. Hutter, S. K. Pathak, F. Niroui, R. H. Friend, M. S. Islam, H. J. Snaith, V. Bulović, T. J. Savenije, S. D. Stranks, *Joule* **2017**, *1*, 155.

[61] D. W. deQuilettes, S. Koch, S. Burke, R. K. Paranji, A. J. Shropshire, M. E. Ziffer, D. S. Ginger, *ACS Energy Lett.* **2016**, *1*, 438.

[62] Y. Li, Y. Zhao, Q. Chen, Y. Yang, Y. Liu, Z. Hong, Z. Liu, Y.-T. Hsieh, L. Meng, Y. Li, Y. Yang, *J. Am. Chem. Soc.* **2015**, *137*, 15540.

[63] A. Merdasa, Y. Tian, R. Camacho, A. Dobrovolsky, E. Debroye, E. L. Unger, J. Hofkens, V. Sundström, I. G. Scheblykin, *ACS Nano* **2017**, *11*, 5391.

[64] F. Bebensee, J. Zhu, J. H. Baricuatro, J. A. Farmer, Y. Bai, H. P. Steinrück, C. T. Campbell, J. M. Gottfried, *Langmuir* **2010**, *26*, 9632.

[65] R. A. Street, J. E. Northrup, B. S. Krusor, *Phys. Rev. B - Condens. Matter Mater. Phys.* **2012**, *85*, 1.

[66] N. H. Nickel, F. Lang, V. V. Brus, O. Shargaieva, J. Rappich, *Adv. Electron. Mater.* **2017**, *3*, 1700158.

[67] F. Lang, O. Shargaieva, V. V. Brus, J. Rappich, N. H. Nickel, *Appl. Phys. Lett.* **2018**, *112*, 081102.

[68] D. R. Ceratti, Y. Rakita, L. Cremonesi, R. Tenne, V. Kalchenko, M. Elbaum, D. Oron, M. A. C. Potenza, G. Hodes, D. Cahen, *Adv. Mater.* **2018**, *1706273*, 1706273.

[69] W. S. Yang, B.-W. Park, E. H. Jung, N. J. Jeon, Y. C. Kim, D. U. Lee, S. S. Shin, J. Seo, E. K. Kim, J. H. Noh, S. Il Seok, *Science* **2017**, *356*, 1376.

[70] D. Macdonald, A. Cuevas, *Appl. Phys. Lett.* **1999**, *74*, 1710.

[71] J. A. Hornbeck, J. R. Haynes, *Phys. Rev.* **1955**, *97*, 311.

[72] H. Hu, D. Wang, Y. Zhou, J. Zhang, S. Lv, S. Pang, X. Chen, Z. Liu, N. P. Padture, G. Cui, *RSC Adv.* **2014**, *4*, 28964.

[73] W. A. Laban, L. Etgar, *Energy Environ. Sci.* **2013**, *6*, 3249.

[74] W. Tress, *Adv. Energy Mater.* **2017**, *7*, 1602358.

[75] W. Li, J. Liu, F. Bai, H. Zhang, O. V Prezhdo, *ACS Energy Lett.* **2017**, *2*, 1270.

[76] Y. Hu, H. Schn, Ø. Nielsen, E. Johannes Øvrelid, L. Arnberg, *J. Appl. Phys.* **2012**, *111*, DOI 10.1063/1.3689786.

[77] W. J. Yin, T. Shi, Y. Yan, *Adv. Mater.* **2014**, *26*, 4653.

[78] G. Landi, C. Barone, C. Mauro, H. C. Neitzert, S. Pagano, *Sci. Rep.* **2016**, *6*, 1.

[79] G. Landi, H. C. Neitzert, C. Barone, C. Mauro, F. Lang, S. Albrecht, B. Rech, S. Pagano, *Adv. Sci.* **2017**, *4*, 1700183.

[80] V. S. Chirvony, S. González-Carrero, I. Suárez, R. E. Galian, M. Sessolo, H. J. Bolink, J. P. Martínez-Pastor, J. Pérez-Prieto, *J. Phys. Chem. C* **2017**, *121*, 13381.

[81] V. S. Chirvony, J. P. Martínez-Pastor, *J. Phys. Chem. Lett.* **2018**, *9*, 4955.

[82] A. M. Goodman, *J. Appl. Phys.* **1961**, *32*, 2550.

[83] T. Dittrich, F. Lang, O. Shargaieva, J. Rappich, N. H. Nickel, E. Unger, B. Rech, *Appl. Phys. Lett.* **2016**, *109*, 073901.

[84] Y. Liu, Z. Yang, S. F. Liu, *Adv. Sci.* **2018**, *5*, 1700471.

[85] M. Saliba, J.-P. Correa-Baena, C. M. Wolff, M. Stolterfoht, N. Phung, S. Albrecht, D. Neher, A. Abate, *Chem. Mater.* **2018**, *30*, 4193.

[86] A. Denker, C. Rethfeldt, J. Röhrich, H. Berlin, D. Cordini, J. Heufelder, R. Stark, A. Weber, B. H. Berlin, *Proc. CYCLOTRONS 2010, (Lanzhou, China)* **2010**, 75.

[87] J. Röhrich, T. Damerow, W. Hahn, U. Müller, U. Reinholz, A. Denker, *Rev. Sci. Instrum.* **2012**, *83*, 02B903.

[88] E. Jones, T. Oliphant, P. Peterson, E. Al., "SciPy: Open source scientific tools for Python," can be found under http://www.scipy.org/, **2001**.